Equid que venihi tasped volut officillum sidit lam p. XX

Quasi volut accae cullit and queomni quis pp. XX & XX

Perspedi cuptatur audicto volut accae cullit p. XX

Science

$15
7 AUGUST 2020
sciencemag.org

AAAS

BUBBLE RUPTURE

Surface tension drives the wrinkling and collapse in viscous fluids p. XXX

FLUID MECHANICS

A new wrinkle on liquid sheets: Turning the mechanism of viscous bubble collapse upside down

Alexandros T. Oratis[1], John W. M. Bush[2], Howard A. Stone[3], James C. Bird[1]*

Viscous bubbles are prevalent in both natural and industrial settings. Their rupture and collapse may be accompanied by features typically associated with elastic sheets, including the development of radial wrinkles. Previous investigators concluded that the film weight is responsible for both the film collapse and wrinkling instability. Conversely, we show here experimentally that gravity plays a negligible role: The same collapse and wrinkling arise independently of the bubble's orientation. We found that surface tension drives the collapse and initiates a dynamic buckling instability. Because the film weight is irrelevant, our results suggest that wrinkling may likewise accompany the breakup of relatively small-scale, curved viscous and viscoelastic films, including those in the respiratory tract responsible for aerosol production from exhalation events.

Wrinkling of thin sheets appears in a variety of settings across a wide range of length scales, including those in neutrophil phagocytosis (*1*), in the development of the epithelial tissue responsible for fingerprints (*2*), and in subduction zones in plate tectonics (*3*). Generally speaking, sheets wrinkle because they require less energy to buckle than to compress when they are subjected to compressive stresses (*4*). Most recent studies have focused on understanding the bending deformations that occur when a thin elastic sheet is stretched (*5*, *6*), poked (*7*, *8*), or wrapped around a curved object (*9*, *10*); however, viscous liquids can also buckle (*11*–*13*). A visually prominent example is the "parachute instability" that develops spontaneously when a bubble rising in a viscous liquid reaches the surface and ruptures (Fig. 1). Bubbles collect at the surface of viscous liquids during processes including glass manufacturing, spray painting (*14*), vitrification of radioactive waste (*15*), and volcanic eruptions (*16*). Having surfaced, the bubble consists of a thin liquid film in the form of a spherical cap that is supported by the gas trapped inside it (Fig. 1A). When the bubble ruptures, the liquid film develops a growing hole that allows the trapped gas to escape. Without the support of this gas, the forces on the liquid film are unbalanced, causing bubble collapse and the development of radial wrinkles around the bubble periphery. Previous investigations have concluded that the wrinkles develop as a consequence of the weight of the collapsing thin film and the geometric constraint imposed by the opening hole (*17*, *18*). We demonstrate here that the wrinkling instability relies on neither gravity nor the presence of the hole.

The development of wrinkles from a collapsing bubble with radius R = 1 cm on a silicone oil bath with viscosity $\mu \approx 10^6$ cP is illustrated in Fig. 1B. The wrinkles emerged in an isolated annular region near the bubble's edge, when the bubble height Z reached a distance of approximately $Z/R \approx 0.6$ from the bath's surface. Before hole formation, the equilibrium shape of a bubble at the air–liquid interface is established by the balance between the pressure excess inside the bubble, ΔP, and a combination of gravitational and capillary forces (*19*). Because the bubble radius in this example is much larger than the capillary length $(\gamma/\rho g)^{1/2} \approx 1$ mm, where γ is the surface tension, ρ the liquid density, and g the acceleration due to gravity, the bubble extends substantially beyond the bath surface and forms a hemisphere. Gravity drives drainage in the thin hemispherical film, causing the bubble walls to thicken toward the base (*17*). Puncturing the film generates a hole and prompts the film retraction from the point of rupture, driven by surface tension and the local curvature of the hole's rim (*20*–*22*). In addition, puncturing the film equilibrates the pressure across the interface, causing $\Delta P \rightarrow 0$. The presence of the hole thus leaves the capillary and gravitational forces acting on the film unbalanced, ultimately causing the bubble collapse. Considering a surface element dA on the spherical cap, the gravitational force acting on the film thickness h scales as $F_g \sim \rho h g dA$, whereas the capillary force pulling the film inward scales as $F_c \sim (4\gamma/R)dA$ (Fig. 1A). For a centimeter-sized bubble with a characteristic thickness of $h \approx 10$ μm, capillary forces (F_c) dominate gravitational forces (F_g) by a factor of $F_c/F_g \sim 4\gamma/(\rho g R h) \approx 80$. This scaling argument indicates that the collapse process is dominated by surface tension rather than gravity.

To test this hypothesis, we conducted an identical experiment after turning the bubble upside down (Fig. 1C). The approach is possible because the liquid is sufficiently viscous that the experiments can be conducted before the silicone oil flows out of the inverted container. We first prepared the bubble right-side up, and then we rapidly rotated the sample and ruptured the bubble within seconds. When inverted, the bubble film (thickness $h \approx 2.4$ μm) maintained its shape and thickened at the

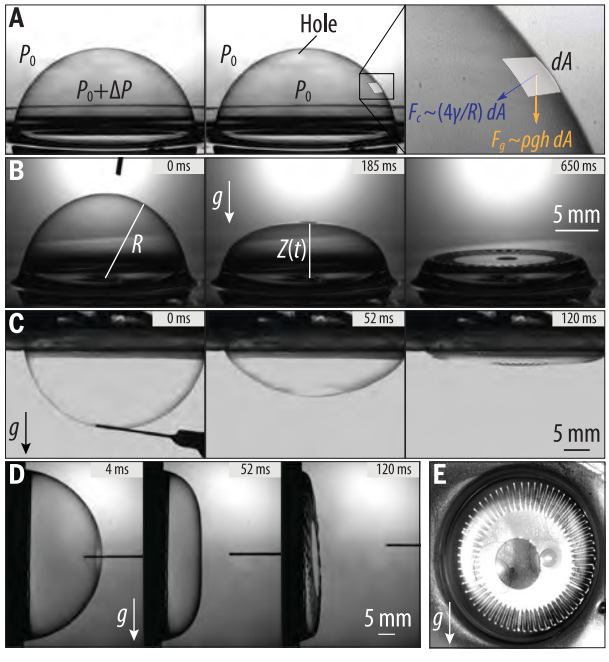

Fig. 1. Collapse of a viscous bubble film upon rupture. (**A**) If a hole develops in the surface of a bubble resting on a liquid surface, then the pressurized air escapes, leaving the gravitational and surface tension forces unbalanced. (**B**) An air bubble with radius R = 1 cm at the surface of a viscous silicone oil bath collapses and its height $Z(t)$ decreases after rupture. As the bubble collapses, wrinkles appear along its periphery. (**C**) When the bubble is rapidly turned upside down and ruptured, it collapses in a similar fashion. (**D** and **E**) Rotating the sample such that its base is parallel to the direction of gravity g results in a similar collapse (D) and wrinkles still appear (E).

[1]Department of Mechanical Engineering, Boston University, Boston, MA 02215, USA. [2]Department of Applied Mathematics, Massachusetts Institute of Technology, Cambridge, MA 02139, USA. [3]Department of Mechanical and Aerospace Engineering, Princeton University, Princeton, NJ 08544, USA.
*Corresponding author. Email: jbird@bu.edu

apex at a rate of ~10 nm/s; therefore, the film geometry does not vary appreciably during either the rotation or inversion (*23*). If gravity and viscosity were the dominant forces, then the inverted bubble would elongate downward, as previously demonstrated in simulations (*24*). Instead, the inverted bubble retracted upward against the force of gravity, and wrinkles formed again during the final stages of bubble collapse (Fig. 1C). The direction of motion clearly demonstrates that gravity does not drive the collapse; however, it does not rule out the possibility that it is involved in the wrinkles. By repeating the experiment with the bubble on its side (Fig. 1D), we found that wrinkles still appeared (Fig. 1E). We thus conclude that gravity plays a negligible role during bubble collapse and wrinkling instability.

To understand the extent to which surface tension drives bubble collapse, we measured the maximum distance of the bubble film $Z(t)$ from the bath surface. From the evolution of the bubble height with time, we can extract a collapse speed $V = dZ/dt$ that will dictate the characteristic time scale of collapse. If surface tension drives the collapse, then it would be expected that the speed would depend on the competing capillary and viscous forces. Indeed, balancing the capillary force γR with the viscous force $\mu h_0 V$ yields a characteristic velocity $V \sim \gamma R/\mu h_0$, where h_0 is the initial film thickness at the apex (*23*). Therefore, we expect the evolution of the bubble height Z and the associated collapse speed V to depend on both the viscosity and thickness of the film. We tested this conjecture through systematic experiments in which we used silicone oils with viscosities of 100, 800, and 3000 Pa • s and also varied the thickness of the film at rupture. Once punctured, the bubble collapsed, decelerating as it reached the bath surface (Fig. 2A). From the high-speed images, we calculated a representative velocity V at the onset of wrinkling by averaging the downward speed dZ/dt over the range $0.6 < Z/R < 1$ (*23*). Increasing the viscosity of the silicone oil slowed down the collapse. As expected, the data collapse when the normalized height Z/R is plotted against the dimensionless time Vt/R (Fig. 2A, inset).

To gain further insight, we determined the rupture thickness at the bubble apex, h_0, by combining optical techniques with the gravitational drainage theory of Debrégeas *et al.* (*17*). Under a monochromatic light, concentric interference fringes could be seen to emanate from the bubble's apex (Fig. 2B, inset). The circles are evidence of axisymmetric drainage, and the rate at which they appear can be measured with thin-film interferometry to estimate the thickness at the apex (*23*). Thinner bubbles collapsed faster (Fig. 2B), as expected from the predicted scaling $V \sim \gamma R/\mu h_0$ (solid line). We acknowledge sizable deviations of the experimental data from this simple scaling, especially for the 100 Pa • s silicone oil bubbles. Nevertheless, the overall trends support the hypothesis that the bubble collapse is driven by surface tension, in which case the characteristic time scale $R/V \sim \mu h_0/\gamma$ becomes independent of the bubble radius.

The model of da Silveira *et al.* (*18*) suggests that gravity and viscosity lead to wrinkling in such a way that the number of wrinkles scales as $n \sim (\rho g R_H^3 \tau_c/\mu h^2)^{1/2}$, with R_H being the radius of the hole and τ_c the time it takes for the film to collapse. The radius of the hole grows rapidly at early times but slows down sufficiently to be adequately modeled as a constant during the instability. This model thus claims that the number of wrinkles depends strongly on the size of the hole, with no wrinkles predicted if $R_H = 0$. To investigate the role of the hole in the development of wrinkles, we performed experiments by drilling a small opening at the bottom of the petri dish in which the silicone oil was placed. We inserted a narrow tube into the opening, injected air to create the bubble, and then sealed the opening with a valve. Once the bubble had reached the surface to create a hemispherical dome, we opened the valve to allow the pressurized air inside the bubble to escape. When the air escaped, $\Delta P \rightarrow 0$, causing the capillary force from the curved surface to be unbalanced and the bubble to collapse (Fig. 3A). Wrinkles again appeared at the final stages of the collapse, indicating that the hole plays a role in wrinkling only by eliminating the pressure difference across the bubble surface (Fig. 3B). We thus need to revisit the wrinkling dynamics to deduce a consistent physical picture for the wrinkling mechanism.

We propose a mechanism in which the wrinkles result when the crushing dynamics of the spherical film lead to a hoop compression that overcomes the smoothing effects of surface tension. Here, the capillary-driven collapse induces a radial velocity in a cylindrical reference frame that scales as $V_r \sim V \sim \gamma R/\mu h_0$ (Fig. 3A). This radial velocity leads to compression rates $\dot{\varepsilon}_{rr}$ and $\dot{\varepsilon}_{\theta\theta}$ in the radial and azimuthal directions, respectively, for the r,θ coordinate system defined in Fig. 3C. For a Newtonian fluid, this compression generates both a radial stress $\bar{\sigma}_{rr}$ and hoop stress $\bar{\sigma}_{\theta\theta}$, which can be related to the rate of radial compression through a Trouton model (*25*), yielding $\bar{\sigma}_{rr} \sim \bar{\sigma}_{\theta\theta} \sim 4\mu h V_r/R$ for a film with thickness h. Here, the overbar denotes that the 3D stress has been integrated over the thickness, leading to a 2D stress with dimensions of force per length. It follows from our scaling for V_r that $\bar{\sigma}_{rr} \sim \bar{\sigma}_{\theta\theta} \sim \gamma h/h_0$ when spatial variation in V_r is neglected. Thus, we expect the crushing kinematics to generate larger compressive stresses at an outer annulus (Fig. 3A, red ring) than at the center because of the larger local film thickness. Regardless of the source of these compressive stresses, surface tension imparts a tensile stress to the liquid sheet that acts to minimize the surface area (Fig. 3D). We believe that the competition of these tensile and compressive stresses is responsible for the location of the wrinkling pattern at a distance L from the center (Fig. 3B). Because the thickness profile is unknown, it is not possible to make a quantitative deduction of the stress field, as would be needed to predict the exact position of the wrinkling pattern. The sheet should remain smooth if surface tension exceeds the compressive stresses throughout the sheet. However, the presence of wrinkles indicates that at a sufficient distance from the center, the

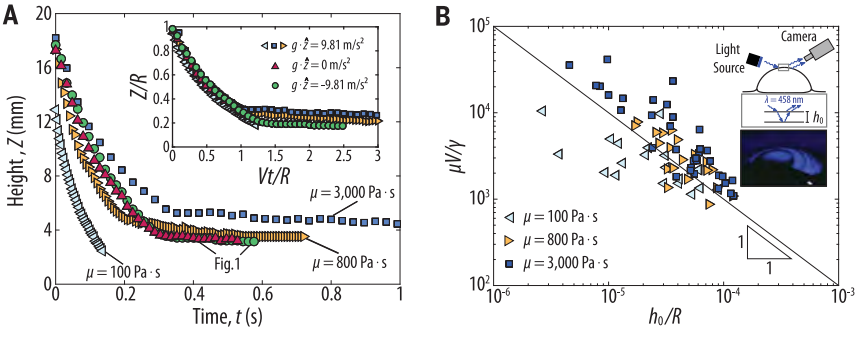

Fig. 2. Effect of bubble film thickness and viscosity on collapse dynamics. (**A**) Measured bubble heights Z versus time t for each orientation and viscosity μ. Inset: The normalized bubble heights Z/R fall onto the same curve when plotted against the dimensionless time Vt/R, highlighting the strong dependence of the collapse speed V on viscosity but not on gravity. (**B**) The collapse speed V is inversely proportional to the measured film thickness h_0, consistent with the notion that surface tension γ drives the collapse. In particular, the experimental results (symbols) suggest that $\mu V/\gamma = 0.1(h_0/R)^{-1}$ (solid line). Here, h_0 is the thickness at the bubble apex, which is estimated using thin-film interferometry (inset).

compressive stresses dominate those acting to keep the sheet smooth. This behavior is analogous to 1D viscous sheets buckling when the rate of compression is faster than the smoothing effect of surface tension (*11*, *13*). To sidestep the theoretical challenges posed by the thickness variation, we approximate the wrinkled region as an annulus of constant thickness h.

To model the development of the wrinkles, we deduced a dynamic version of the first Föppl–von Kármán equation (*23*, *26*, *27*), which describes the normal force balance along the sheet's center line $\zeta(r, \theta, t)$ as follows (Fig. 3D):

$$\rho h\frac{\partial^2\zeta}{\partial t^2}+\frac{\mu h^3}{3}\nabla^4\left(\frac{\partial\zeta}{\partial t}\right)-\bar{\sigma}_{rr}\frac{\partial^2\zeta}{\partial r^2}-\frac{1}{r^2}\bar{\sigma}_{\theta\theta}\left(\frac{\partial^2\zeta}{\partial\theta^2}+r\frac{\partial\zeta}{\partial r}\right)=2\gamma\nabla^2\zeta \quad (1)$$

where ∇^4 is the biharmonic operator and ∇^2 the Laplacian. Motivated by the observation of multiple radial wrinkles, we sought solutions of the form $\zeta(r, \theta, t) = f(r)\exp(\omega t + in\theta)$. Here, $f(r)$ determines the radial variation of the wrinkle amplitude, ω is the wrinkle growth rate, and n the number of wrinkles. In terms of these parameters, Eq. 1 becomes:

$$\left[\rho h\omega^2 f\right]+\left[\frac{\omega\mu h^3}{3}\left\{\frac{1}{r}\frac{d}{dr}\left(r\frac{d}{dr}\right)-\left(\frac{n^2}{r^2}\right)\right\}^2 f\right]-\left[(\bar{\sigma}_{rr}+2\gamma)\frac{d^2f}{dr^2}+(\bar{\sigma}_{\theta\theta}+2\gamma)\left(\frac{1}{r}\frac{d}{dr}-\frac{n^2}{r^2}\right)f\right]=0 \quad (2)$$

The three square-bracketed terms in Eq. 2 correspond, respectively, to inertia, bending, and compression. Given the high viscosity of the film, one might be tempted to neglect inertial effects. However, the rate of wrinkle development, ω^{-1}, is ~10 ms (Fig. 3E), sufficiently short for the inertial term to become non-negligible. Indeed, for a typical thickness $h \approx 10$ μm, we found the ratio of the inertial and radial compression terms to be of order $\rho h R^2\omega^2/\gamma \sim 1$, justifying the inclusion of inertia in Eq. 1.

When considering axisymmetric film effects, the radial stress $\bar{\sigma}_{rr}$ can have a pronounced role in wrinkling caused by the release of azimuthal stress $\bar{\sigma}_{\theta\theta}$ as the wrinkles develop (*6*). As the dominant stress changes from azimuthal to radial, the dependence on n in the dominant terms of Eq. 2 also changes. Scaling relationships for the growth rate ω and the number of wrinkles n can be obtained from a dominant balance. Specifically, the inertial term scales as $\rho h\omega^2$, the azimuthal bending as $\omega n^4\mu h^3/R^4$, and the radial stress component as γ/R^2. The simultaneous balance of these three dominant terms yields a growth rate $\omega^{-1} \sim \sqrt{\rho h R^2/\gamma}$ and the number of wrinkles $n \sim (2\gamma R^2/\omega\mu h^3)^{1/4}$, or equivalently:

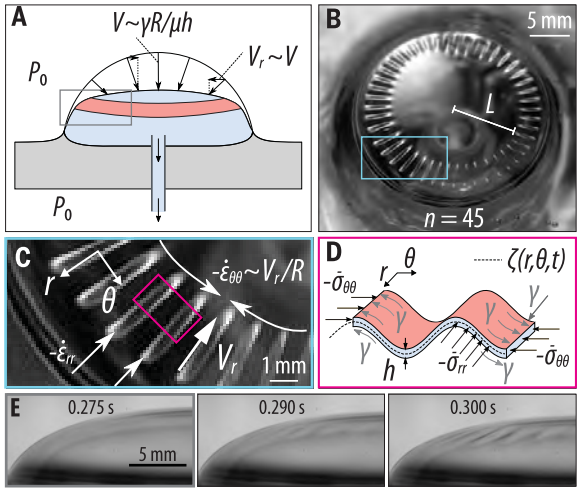

Fig. 3. Mechanism for bubble collapse without rupture. (**A**) Schematic illustrating the experimental setup used to collapse the bubble without rupture. As the bubble collapses, the viscous film obtains a radial velocity V_r proportional to the collapse speed V. (**B**) Wrinkles can still appear without the presence of the hole at a radial distance L from the center. (**C**) Near the periphery of the bubble, the radial and azimuthal compression rates, $\dot{\varepsilon}_{rr}$ and $\dot{\varepsilon}_{\theta\theta}$, respectively, can be related to the radial velocity V_r. (**D**) The azimuthal rate of compression leads to compressive stresses $\bar{\sigma}_{rr}$ and $\bar{\sigma}_{\theta\theta}$, which tend to bend the sheet's centerline $\zeta(r, \theta, t)$ despite being opposed by surface tension γ, which acts to smooth the surface. (**E**) As the bubble collapses, the wrinkles grow and develop within ~25 ms.

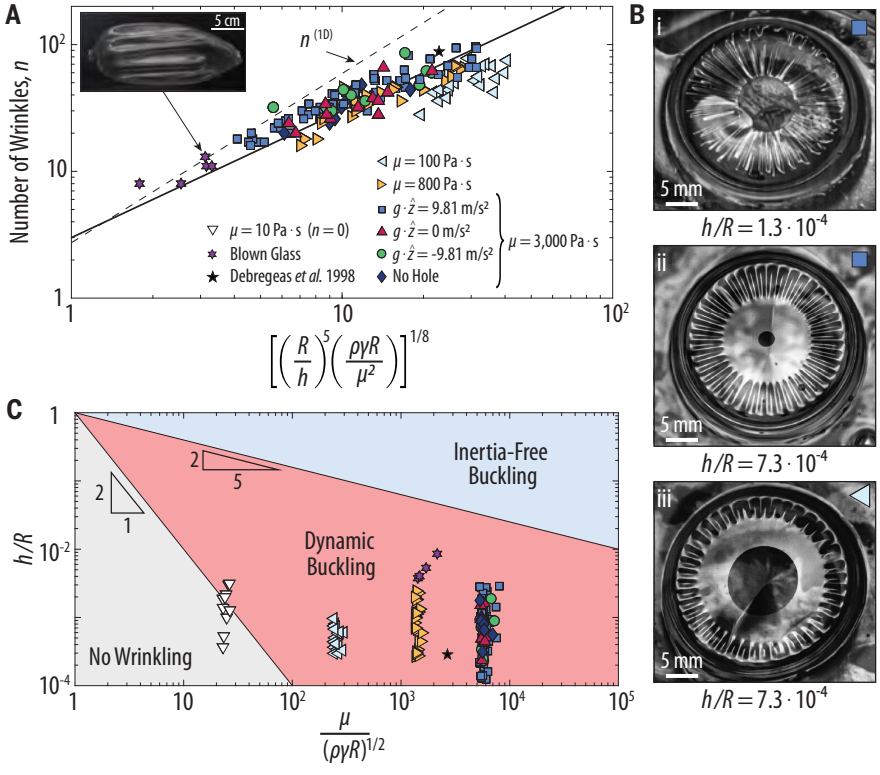

Fig. 4. Comparison of data and model predictions. (**A**) Number of wrinkles n observed on bubbles of various orientations and viscosities is in satisfactory agreement with the scaling of Eq. 3. Wrinkles on blown glass (inset) are also consistent with this trend, although the 1D hoop model (dashed line) is expected to be more appropriate for this nearly cylindrical geometry. (**B**) Top-view images of wrinkled films for: (**i**) viscosity μ = 3000 Pa • s and aspect ratio $h/R = 1.3 \cdot 10^{-4}$, (**ii**) μ = 3000 Pa • s and $h/R = 7.3 \cdot 10^{-4}$, and (**iii**) μ = 100 Pa • s and $h/R = 7.3 \cdot 10^{-4}$. The radial extent of the wrinkles for the thinnest films is limited by the size of the hole, whereas the location L of wrinkles generally increases as the film viscosity decreases. (**C**) Our analysis predicts that inertia is negligible only when $\mu/\sqrt{\rho\gamma R} \gtrsim (R/h)^{5/2}$ (blue region). Because all available data (symbols) are outside of this regime, we incorporated inertial effects into our model. The analysis predicts that there is insufficient growth time for wrinkles to develop when $\mu/\sqrt{\rho\gamma R} \lesssim (R/h)^2$ (gray region), consistent with no wrinkles being observed at the lowest film viscosity (white triangles). Here, the thickness h is computed using the collapse speed V through the relation $h = \gamma R/\mu V$.

$$n \sim \left[\left(\frac{R}{h}\right)^5 \left(\frac{\rho\gamma R}{\mu^2}\right)\right]^{1/8} \quad (3)$$

To test the scaling of Eq. 3 for the number of wrinkles, we conducted systematic experiments in which we varied the bubble viscosity and orientation while keeping the bubble size confined to the range $0.8 < R < 2$ cm. We also repeated the experiments that involved evacuation rather than puncture of the bubble. We estimated the wrinkled film thickness h using the collapse time $R/V \equiv \mu h/\gamma$, which yields a result that is approximately an order of magnitude larger than the apex thickness h_0 (Fig. 2C). Furthermore, we performed additional experiments with thicker structures by extracting blown molten glass from a furnace and allowing the trapped air to escape through the glass-blowing pipe (*23*). As the air escaped, the blown glass collapsed and adopted a wrinkled shape with thickness $h \approx 200$ μm (Fig. 4A, inset).

The experimental results for the number of wrinkles are illustrated in Fig. 4A. Depending on the initial radius, thickness, and viscosity, the number of wrinkles can range between eight and 96. The experimental results (data points) are in fair agreement with our theoretical prediction (solid line) from Eq. 3. A limitation of our model applies to the data with the thinnest films. For these bubbles, the collapse was so abrupt that the wrinkling pattern lost its symmetry and the wrinkles spanned the entirety of the bubble (Fig. 4Bi). In addition, one should be cautious when interpreting the data for the 100 Pa • s bubble films given the discrepancy evident in Fig. 2B. This discrepancy may stem in part from variations in the thickness profile, which may explain the larger hole size and wrinkle location L observed at this lower viscosity (Fig. 4, Bii and Biii). Note that our analysis is based on the assumption that the wrinkle location L is proportional to the bubble radius and does not account for any dependence of L on film thickness or viscosity.

Our model assumes that the wrinkles develop on an axisymmetric portion of a spherical shell, which may be less appropriate for the blown glass. Specifically, because the molten glass was constantly rotated as it was worked into a thin film, the molten glass bubble (Fig. 4A, inset) assumed the form of a cylindrical shell with roughly hemispherical caps before collapse, and a wrinkled cylinder thereafter. For this case, in solving Eq. 2, we considered a hoop with radius R, where the amplitude f is approximately constant. This approach yields the 1D dynamic buckling dispersion relation $\rho h\omega^2 + \omega\mu h^3 n^4/3R^4 - \bar{\sigma}_{\theta\theta} n^2/R^2 = 0$ (*23*). Linear stability analysis revealed that the most unstable wrinkling pattern is then associated with a growth rate $\omega^{(1D)} \sim (\gamma^2/\rho\mu h^4)^{1/3}$ and a number of wrinkles $n^{(1D)} \sim [(R/h)^5(\rho\gamma R/\mu^2)]^{1/6}$, results analogous to those of Howell (*26*). Although the number of experiments performed with blown glass was insufficient to draw a definitive conclusion, we expect the 1D scaling (Fig. 4A, dotted line) to be more appropriate for this nearly cylindrical geometry. The 2D disk scaling of Eq. 3 is more convincing for all of the data involving the spherical cap bubble geometry.

A prediction of our model is that wrinkling will not occur for all conditions. In both the 1D and 2D scaling, inertia played a critical role in determining the number of wrinkles. Indeed, in both cases, inertia was relevant when $n > 1$, or equivalently $h/R < (\mu/\sqrt{\rho\gamma R})^{-2/5}$, a criterion satisfied by all of our data (Fig. 4C). For the 1D model, had inertia been neglected, the resulting buckled profile would be the equivalent of Euler buckling for a straight beam (*23*). Inertia also appears to dominate the instability growth rate ω: We found no evidence that the viscosity influenced this growth rate time, consistent with our model (*23*). For wrinkles to develop, the time scale for them to grow, $\sqrt{\rho h R^2/\gamma}$, must be less than that of collapse, $\mu h/\gamma$. We thus predict that no wrinkling will occur when $h/R < (\mu/\sqrt{\rho\gamma R})^{-2}$. To test this hypothesis, we ruptured bubbles formed from a silicone oil with viscosity $\mu = 10$ Pa • s (Fig. 4C, white triangles) and indeed found that they did not support any wrinkles.

We have demonstrated that surface tension rather than gravity drives the collapse of viscous surface bubbles after rupture and is likewise responsible for the parachute instability. The capillary-driven collapse initiates a dynamic buckling instability prescribed by the simultaneous interplay of inertia, compression, and viscous bending of the retracting film. Our results suggest that analogous wrinkling is likely to arise on relatively small, curved films, where the effects of gravity are entirely negligible. Equation 1, governing the number of wrinkles, is the viscous counterpart of the elastic Föppl–von Kármán equations used to study the deformation of elastic plates and shells. Our system thus presents an example of viscous sheets exhibiting elastic-like instabilities when rapidly compressed. On the basis of the similar roles played by viscosity and elasticity in these two systems, we can foresee extending our model to systems involving viscoelastic films, in which viscoelastic, capillary, and inertial effects all contribute to the dynamics. For instance, the exhalation of potentially pathogen-bearing aerosols has been linked to the breakup of thin bubble films in the viscoelastic fluid lining of the respiratory tract (*28*, *29*). Our deduction that surface tension alone may prompt buckling during viscous film rupture and retraction suggests the possibility of these films folding and entrapping air, thereby enriching the aerosolization process.

REFERENCES AND NOTES

1. M. B. Hallett, S. Dewitt, *Trends Cell Biol.* **17**, 209–214 (2007).
2. M. Kücken, A. C. Newell, *EPL* **68**, 141–146 (2004).
3. L. Mahadevan, R. Bendick, H. Liang, *Tectonics* **29**, n/a (2010).
4. D. P. Holmes, *Curr. Opin. Colloid Interface Sci.* **40**, 118–137 (2019).
5. J. Huang *et al*., *Science* **317**, 650–653 (2007).
6. B. Davidovitch, R. D. Schroll, D. Vella, M. Adda-Bedia, E. A. Cerda, *Proc. Natl. Acad. Sci. U.S.A.* **108**, 18227–18232 (2011).
7. D. Vella, A. Ajdari, A. Vaziri, A. Boudaoud, *Phys. Rev. Lett.* **107**, 174301 (2011).
8. D. Vella, J. Huang, N. Menon, T. P. Russell, B. Davidovitch, *Phys. Rev. Lett.* **114**, 014301 (2015).
9. H. King, R. D. Schroll, B. Davidovitch, N. Menon, *Proc. Natl. Acad. Sci. U.S.A.* **109**, 9716–9720 (2012).
10. J. Hure, B. Roman, J. Bico, *Phys. Rev. Lett.* **109**, 054302 (2012).
11. G. I. Taylor, in *Proceedings of the Twelfth International Congress of Applied Mechanics, Stanford, 1968* (Springer, 1969), pp. 382–388.
12. J. Teichman, L. Mahadevan, *J. Fluid Mech.* **478**, 71–80 (2003).
13. M. Le Merrer, D. Quéré, C. Clanet, *Phys. Rev. Lett.* **109**, 064502 (2012).
14. M. Kadoura, N. Saranjam, S. Chandra, H. Fan, *Prog. Org. Coat.* **99**, 452–462 (2016).
15. R. Pokorny *et al*., *J. Am. Ceram. Soc.* **98**, 3112–3118 (2015).
16. H. M. Gonnermann, M. Manga, *Annu. Rev. Fluid Mech.* **39**, 321–356 (2007).
17. G. Debrégeas, P.-G. de Gennes, F. Brochart-Wyart, *Science* **279**, 1704–1707 (1998).
18. R. da Silveira, S. Chaıeb, L. Mahadevan, *Science* **287**, 1468–1471 (2000).
19. Y. Toba, *J. Oceanogr. Soc. Jpn* **15**, 121–130 (1959).
20. F. Culick, *J. Appl. Phys.* **31**, 1128–1129 (1960).
21. G. Debrégeas, P. Martin, F. Brochard-Wyart, *Phys. Rev. Lett.* **75**, 3886–3889 (1995).
22. N. Savva, J. W. M. Bush, *J. Fluid Mech.* **626**, 211–240 (2009).
23. See the supplementary materials.
24. N. M. Ribe, *J. Fluid Mech.* **457**, 255–283 (2002).
25. F. T. Trouton, *Proc. R. Soc. London A Contain. Pap. Math. Phys. Character* **77**, 426–440 (1906).
26. P. D. Howell, *Eur. J. Appl. Math.* **7**, 321–343 (1996).
27. S. Bhattacharya, R. V. Craster, M. R. Flynn, *Phys. Fluids* **25**, 043102 (2013).
28. G. R. Johnson, L. Morawska, *J. Aerosol Med. Pulm. Drug Deliv.* **22**, 229–237 (2009).
29. J. B. Grotberg, *Phys. Fluids* **23**, 21301 (2011).

ACKNOWLEDGMENTS

We thank P. Houk for blowing the ultrathin glass bubbles and the referees who urged us to consider a 2D model, which we believe led to a substantially improved manuscript. **Funding:** This work was supported by National Science Foundation grant nos. 1004678 and 1351466 and Office of Naval Research grant no. N00014-16-1-3000. **Author contributions:** A.T.O., J.W.M.B., H.A.S., and J.C.B. designed the study. A.T.O. and J.C.B. conducted the experiments and acquired the data. A.T.O., J.W.M.B., H.A.S., and J.C.B. interpreted the data and proposed mechanical models. A.T.O., J.W.M.B., H.A.S., and J.C.B. contributed equally to the final version of the manuscript. **Competing interests:** The authors declare no competing interests. **Data and materials availability:** All data are available in the main text or the supplementary materials.

SUPPLEMENTARY MATERIALS

science.sciencemag.org/content/369/6504/685/suppl/DC1
Materials and Methods
Figs. S1 to S10
Table S1
References (*30*–*37*)
Movies S1 to S8
Experimental Data Files

12 November 2019; accepted 25 June 2020
10.1126/science.aba0593